On the impact of H_2-enrichment on flame structure and combustion dynamics of a lean partially-premixed turbulent swirling flame

P. W. Agostinelli[a,b,*], D. Laera[b], I. Chterev[c], I. Boxx[c], L. Gicquel[b], T. Poinsot[d]

[a] *Safran Helicopter Engines, 64510 Bordes, France*
[b] *CERFACS, 42 avenue Gaspard Coriolis, 31057 Toulouse, France*
[c] *Institut für Verbrennungstechnik, Deutsches Zentrum für Luft-und Raumfahrt (DLR), Stuttgart, Germany*
[d] *Institut de Mécanique des Fluides de Toulouse, IMFT, Université de Toulouse, CNRS, Toulouse 31400, France*

Abstract

Large Eddy Simulation (LES) with Conjugate Heat Transfer (CHT) is used to analyze the impact of H_2-enrichment on the flame structure and combustion dynamics of a lean partially-premixed turbulent CH_4/Air swirling flame. Experimentally, the combustor is operated at atmospheric pressure with H_2 fuel fractions of up to 50%, by volume. LES-CHT results are compared and validated against time-resolved stereo PIV, OH* chemiluminescence, OH-PLIF imaging and acoustic pressure measurements. In terms of dynamics, for the pure CH_4 and 20% of H_2 enrichment cases, no thermoacoustic oscillation is observed in either the experimental or numerical data. As the fuel fraction of hydrogen is increased, the flame length reduces due to the increase in laminar flame speed and the heat release rate distribution becomes more compact. CHT simulations reveal that H_2-enrichment leads to higher temperatures at the centerbody tip. At 50% H_2, in agreement with experiments, LES predicts a bi-modal thermoacoustic oscillation, with two main frequencies corresponding to the quarter and chamber modes of the system. Dynamic Mode Decomposition is performed on the measured OH-PLIF images and LES 3D fields to extract each mode contribution to the overall flame dynamics. It is observed that both modes are characterized by local variations of equivalence ratio, while only the higher frequency (chamber) mode is characterized by vortices periodically detaching from the backplane and the centerbody walls causing a strong periodic wrinkling of the flame front during the thermoacoustic oscillation.

Keywords: H_2-enrichment, Thermoacoustic instabilities, Large Eddy Simulation, Turbulent flames, Conjugate Heat Transfer

*Corresponding author: agostinelli@cerfacs.fr

1. Introduction

Hydrogen is rapidly becoming one of the most exciting topics of discussion in the combustion community [1, 2, 3]. Although aeronautical and power generation industries have reached low emission levels with conventional fuels [4, 5, 6], both are considering hydrogen and hydrogen-rich gases (e.g. syngas) as a solution to reduce their impact on the environment to comply with European Union future regulations on emissions. An appealing strategy prior to fuel decarbonization is to implement H_2 in existing or modified gas turbines [7]. However, the different chemical properties of H_2 compared to classical hydrocarbon fuels must be accounted for when considering this type of application. The high reactivity of hydrogen and its wide flammability range [8, 9] together with the high flame speed [10] can enhance the flame stabilization at lower equivalence ratios but, at the same time, it can increase the risk of unwanted phenomena such as flashback [11, 12] or thermoacoustic instabilities [13, 14, 15, 16].

For laminar flames, multiple numerical and experimental studies demonstrate the impact of H_2-enrichment in CH_4/air flames through the change of the mixture laminar flame speeds [17, 18, 19], lean blow-off and extinction limits [20, 21] or potential changes in stabilization mechanisms or instabilities [22]. In the experimental work of Schefer *et al.* [23], the effect of hydrogen addition on the flame stability and blowout for a lean premixed swirl-stabilized methane/air flame showed that hydrogen addition increases the peak OH concentration which leads to a significant change in the flame structure: it becomes shorter and more robust. A similar hydrogen addition effect is observed by Cozzi *et al.* [24] in a non-premixed unconfined configuration featuring a swirling flow: a shorter flame stabilized closer to the burner is obtained when hydrogen enrichment is considered. Flame stabilization has been analyzed by Guiberti *et al.* [25] and Shanbhogue *et al.* [26], showing that the probability of stabilizing confined swirled M-flame increases with H_2 concentration in the fuel mixture. Similar conclusions have been found also in other studies, e.g. Refs. [27, 28, 29, 30, 31]. Numerically, recent work by Laera *et al.* [32] analyzes the case of a direct H_2 injection through a pilot lance typical of land-based gas turbines or aeroengines [6], opening new questions on the resulting flame structure and stabilization mechanisms, highlighting the importance of transport property modeling when dealing with hydrogen, a well-known issue for classical single-fuel systems [33]. In all these studies, the flame clearly approaches the combustor walls so the thermal load on the combustor walls increases, underlining the importance of the thermal boundary conditions in controlling H_2-enriched flames. In numerical investigations, this renders impossible the use of simplified thermal wall treatments such as imposing adiabaticity [34] or an arbitrary wall temperature field [35, 36, 37] when H_2-enriched flames are investigated. A more complex and realistic Conjugate Heat Transfer (CHT) approach should instead be preferred as recently discussed by multiple studies [38, 39, 40, 41]. A more comprehensive discussion on the heat transfer modeling for the accurate numerical prediction of swirled-stabilized flames dynamics could be found in Ref. [39].

A comprehensive review on the effect of hydrogen addition on flame dynamics and thermoacoustic instabilities for gas turbine application has been recently presented by Beita *et al.* [42] so only some of the recent publications are hereafter reported. In brief, hydrogen modifies the flame shape, altering the gain and phase of the corresponding Flame Transfer Function (FTF), e.g. Refs. [43, 44, 45, 46]. As a result, hydrogen addition can affect self-sustained combustion instabilities in a variety of (seemingly) contradictory ways based on the conditions in which the analyses are performed. Multiple studies show that variations in hydrogen content can cause a shift in the acoustic modes of combustors [47, 48, 49, 50, 51] or flame shape promoting self-sustained oscillations in longitudinal [26, 30, 52, 53, 13, 54] and annular combustors [55, 56]. Other studies observe a stabilization of the oscillations when hydrogen is added, e.g. Refs. [57, 7, 58]. Kang and Kim [59] demonstrate that lean-premixed and ultra-compact pure hydrogen flames can trigger high-frequency instabilities while the system remains completely stable in the low frequency range. Similar results have been found also by Taamallah *et. al* [60]. Recently, Datta *et al.* [61] and Kushwaha *et al.* [62] analyzed the impact of hydrogen enrichment on the dynamics of methane swirled-stabilized flames, pointing out that hydrogen enrichment can trigger limit cycle as well as chaotic or intermittent thermoacoustic oscillations. From numerical investigations, in agreement with experimental finding, Nam and Yo [57] show that adding hydrogen can inhibit a thermoacoustic instability. A doubling of the oscillation amplitude of high-frequency modes is observed in numerical simulations of a full scale DLE burner from Siemens for when the low frequency instability is damped by hydrogen enrichment [63]. These few examples do not show however a thorough comparison with experiments and a complete evaluation of the state of the art LES modeling. Therefore, despite the large potential of Large Eddy Simulation (LES) in predicting reactive flows in complex industrial configurations [64, 65, 66, 67], numerical simulations have not been extensively used to predict burner acoustic stability due to H_2 addition and research is still needed.

This work proposes high-fidelity LES to fully analyze the impact of H_2-enrichment on flame shape and stabilization, thermal load on combustor components as well as flame thermoacoustic dynamics while evaluating state of the art LES modeling in this specific context and validating the predictions against a full set of high-quality experimental data. Note that for our work, the simulations are compared to experiments performed using the PRECCINSTA gas turbine model combustor [68, 69] operated with methane with up to 50% hydrogen admixture (by volume). On the modeling side, to account for heat-transfer and analyze the effect of H_2 addition on the burner thermal load, CHT simulations are performed by coupling the AVBP LES solver with the AVTP heat-conduction solver [70, 71]. For the CH_4-H_2/Air combustion, an Analytically Reduced Chemistry (ARC) mechanism is employed (see Supplementary Material) together with a dynamic formulation of the Thickened Flame LES (DTFLES) combustion model [72]. The experimental and the numerical setups are presented in section 2. Experimental measurements and numerical predictions are then detailed in section 3. In terms of dynamics, the 0% H_2 and the 20% H_2 (stable) flames are presented in sections 3.1 and 3.2, respectively. The 50% H_2 flame, which exhibits bi-modal thermoacoustic oscillations, is presented in section 3.3. Finally, the effect of H_2 addition on the flame stabilization and shape (section 4.1), the thermal load and fluid temperature (section 4.2) as well as the flame dynamics (section 4.3) are discussed.

2. Experimental and numerical setups

2.1. The PRECCINSTA combustor

The PRECCINSTA gas turbine combustor operated by DLR [68] is presented in Fig. 1(a) illustrating the injector, the combustion chamber and the normalized time-averaged Line-of-sight (LOS) OH* chemiluminescence image for the reference pure CH_4 flame. In this setup, dry air is fed at ambient temperature through the plenum and 12 radial swirl channels impose a swirling motion to the flow before entering the combustion chamber. The fuel is injected into the air stream through 12 small holes located within the radial swirler in a "technically premixed" mode, i.e. in a manner similar to how one would achieve premixing in a technical combustor system [68]. Thanks to the high momentum, a good air/fuel mixing is ensured before entering the combustion chamber although local equivalence ratio variations have been observed in previous studies both in thermoacoustically stable and unstable conditions [68, 39, 73]. The combustion chamber has a square section of 85 x 85 mm^2 and quartz windows (thickness 1.7 mm) to allow for optical access for diagnostics. At the end of the combustion chamber, the hot gases exit through a cone-shaped exhaust pipe. Several laser diagnostic techniques are applied in this study. Using Stereoscopic Particle Image Velocimetry (sPIV), measurements of the three velocity components are performed in the axial-radial plane of the combustion chamber. Planar Laser-Induced Fluorescence (PLIF) measurements of OH radicals are also performed to visualize the flame structure together with LOS integration of OH* chemiluminescence. Note that OH* chemiluminescence is a commonly accepted, qualitative proxy for heat release in lean, premixed hydrocarbon flames [74, 75, 76, 77, 78], and has been used extensively to characterize the release dynamics in the PRECCINSTA burner [79, 68, 80, 81, 82, 83, 84].

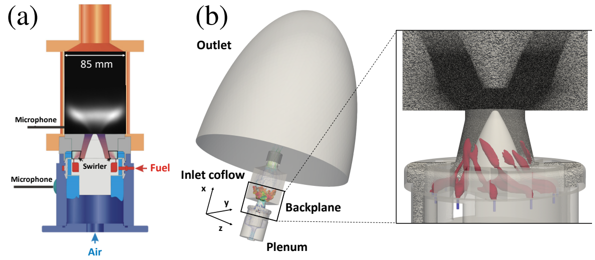

Figure 1: (a) Schematic of the PRECCINSTA: injector with combustion chamber and normalized time-averaged line-of-sight (LOS) OH* chemiluminescence for the pure CH_4 flame. (b) Computational domain used in LES with overview of the fluid mesh. The instantaneous isocontour of CH_4 (colored in red) helps visualize the technical injection of the fuel in the swirled flow.

Different experimental [68, 85, 86, 69, 62, 61] and numerical [73, 87, 88, 35, 89, 90, 91, 92, 93, 94, 95, 96, 39] studies have been carried out to analyze swirl-stabilized flames of methane and natural gas in the PRECCINSTA test bench. First analyses of the thermoacoustic oscillations were performed via compressible LES by Roux *et al.* [89] and Franzelli *et al.* [73], achieving good prediction of the oscillation. Fredrich *et al.* [88, 95] also recently detected the reported thermoacoustic instability with a fully-compressible LES-pdf approach achieving even better prediction of the oscillation frequency. More studies focused on the impact of detailed chemistry [87], sub-grid scale closure for premixed turbulent combustion [92], combustion DTFLES

Case	H_2 [% fuel vol.]	$\dot{m}_{air}$ [g/s]	$\dot{m}_{CH_4}$ [g/s]	$\dot{m}_{H_2}$ [g/s]	ϕ	P_{th} [kW]	s_L [m/s]	T_{ad} [K]
A	0%	4.29	0.2	-	0.8	10	0.26	1997
B	20%	4.23	0.186	0.006	0.8	10	0.30	2006
C	50%	4.12	0.154	0.019	0.8	10	0.42	2030

Table 1: Summary of the operating conditions considered in the present work.

model with a dynamic wrinkling formulation [94] and mesh sensitivity [35, 96]. An analysis of the wall heat transfer impact on the thermoacoustic behavior of this test rig has since then been performed, showing that stable flame prediction in agreement with experiments can be achieved only with CHT simulations [39][1].

Experimentally and very recently, the rig has been operated with different H_2-enrichment levels (up to 50% in volume) to analyze the effect on the flame dynamics and the flame stabilization process. Results of this test campaign on the flame stabilization and dynamics have been presented in recent publications by Datta *et al.* [61] and Kushwaha *et al.* [62], respectively. Starting from these results, the present article presents LES simulations to complement experimental observations and gain in physical understanding by focusing on a smaller set of operating conditions and quantifying the effect of hydrogen addition on the flame stabilization and its dynamics as well as the thermal load on the combustor walls. The operating conditions considered for a global equivalence ratio of ϕ = 0.8 and a thermal power of P_{th} = 10kW are summarized in Table 1. Case *A* refers to the condition without hydrogen admixture [39]. Cases *B* and *C* refer to flames fueled by methane with 20% and 50% admixture of hydrogen (by volume), respectively. Note that, experimentally, whereas Cases *A* and *B* were quite stable, Case *C* experienced significant thermoacoustic oscillation.

2.2. LES numerical setup

Figure 1(b) presents the computational domain used in this study. The inlet fuel geometry is simplified into 12 small tubes (colored in blue) without the fuel plenum: to help visualize the technical fuel injection in the swirled flow, an instantaneous isocontour of CH_4 is shown in red. LES is performed using the AVBP code (cerfacs.fr/avbp7x/index.php) solving the compressible Navier-Stokes multi-species equations. The TTGC scheme (third order in time and space) is used for the discretization of the convective terms [97] and the SIGMA turbulent closure is used for the sub-grid stresses [98]. The LES computational grid consists of 76M tetrahedral cells. Note that the grid was refined in the flame region applying static mesh adaptation criteria [96]. The final mesh has a characteristic size in the flame zone just downstream of the centerbody tip of Δ_x = 200 μm assuring a y^+ value lower than unity at the centerbody tip and $y^+ \sim 3$ at the chamber and backplane walls, hence allowing the use of a wall resolved LES approach (no slip conditions on all walls) and a reasonable estimation of the thermal boundary layer[2]. H_2-enrichment, in comparison to conventional fuel flames, is known to reduce the flame thickness making it difficult to resolve the flame front on the computational grid while requiring reasonable High Performance Computing (HPC) resources. In terms of modeling, in the following, the dynamic formulation of the thickened flame model (DTFLES) [72] is used. Since a thickened reactive layer is less sensitive to turbulence, an efficiency function Ξ_Δ is introduced to compensate for the corresponding reduction of the flame surface [97, 100]. Note that following previous work of Volpiani *et al.* [94] on the same configuration, a dynamic formulation of the Charlette efficiency function [100] is used to allow an on-the-fly local estimation of the model parameter β_{Ch}. CH_4-H_2/Air was modelled using a novel Analytically Reduced Chemistry (ARC) mechanism consisting of 18 transported species, 144 reactions, and 12 quasi-steady state species, derived from the detailed PoliMi scheme [101] using ARCANE [102]. This kinetic scheme has been validated through Cantera (www.cantera.org) calculations of a 1D-premixed and 1D-counterflow flames against experimental data and detailed schemes (see Supplementary Material). This approach is chosen over more conventional 2 step schemes because of the need to consider different bi-fuel mixture compositions. Note also that the transport property model here used is the simplified one that consists of determining the viscosity using Sutherland's law, in deducing the mixture heat conductivity from a constant Prandtl number and in computing each species diffusivity based on a constant Schmidt

[1]Most studies have analyzed the stable flame (equivalence ratio ϕ = 0.83 and thermal power P_{th} = 30kW) and the unstable flame experiencing a thermoacoustic limit cycle at 290 Hz (ϕ = 0.7 and P_{th} = 25 kW) as reported by Meier *et al.* [68].

[2]Note that, for the used value of y+, the first point of the mesh is located in the viscous sub layer, where the velocity profile is almost linear. This allows for a correct estimation of the velocity boundary layer, and therefore of the friction at the wall. For substances such as air, the thermal boundary layer is even larger than the velocity boundary layer, being the Prandtl number below one [99]. In the present case, the Prandtl number reads 0.69, leading to a thermal boundary layer thickness larger than the velocity one. This means that the thermal boundary layer is even more easily resolved than the hydrodynamic layer, assuring a correct estimation of the heat transfer at the wall.

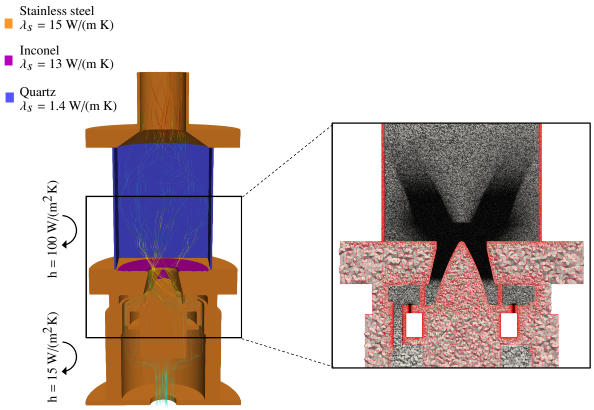

Figure 2: Computational domain used in CHT simulations with overview of the solid (red) and fluid (black) meshes. Assumed thermal boundary conditions and thermal conductivities λ_s are indicated [39].

number specific for each species. Hence, the use of the simplified model takes into account the non-unity Lewis number and the different species diffusivity but neglects the Soret effect and the variations of the Schmidt and the Prandtl number which are marginal for the H_2 molar fraction here considered [32]. Inlet and outlet boundary conditions are treated with the Navier-Stokes Characteristic Boundary Conditions (NSCBC) [103] with a relaxation factor of $K_{air} = 50\ \mathrm{s}^{-1}$ and $K_{fuel} = 5 \times 10^5\ \mathrm{s}^{-1}$ imposed on the air and fuel inlets[3], respectively [39].

At the same time, heat-transfer at the walls is accounted for with the CHT approach, by coupling the AVBP LES code with the AVTP solid conduction code [70, 71]. In such a case, AVBP and AVTP run in parallel and exchange the solid surface temperature T_s and the heat flux Φ_q at the boundaries. The CHT computational domain is shown in Fig. 2 where the solid mesh is indicated in red and the fluid one is in black. The solid parts are discretized using 16M tetrahedral elements and a resolution of at least 5 points across the thin chamber walls. For the conduction case, an implicit first-order Euler scheme is used for time integration and a second-order Galerkin diffusion scheme is applied for spatial discretization. Heat fluxes at the solid boundaries in contact with the fluid are determined from the LES solution. For example, the centerbody surface temperature, which is critical for flame root stabilization, is the result of the balance between the heat taken from the hot flow at the centerbody tip and the heat given to the fresh gases along the walls. Thermal boundary conditions must instead be indicated for the surfaces of the solid not in contact with the fluid domain (e.g. external chamber walls, external plenum walls). The required heat exchange coefficients at these boundaries have been determined for the external side of the chamber and plenum walls (Fig. 2). Finally, thermal radiation from the hot gases is taken into account by the AVBP LES solver through an Optically Thin Assumption (OTA) [104] for the most radiating species CH_4, CO, CO_2, and H_2O: gases are assumed to be optically thin and re-absorption is neglected while the Planck mean-absorption coefficients are provided for each species as polynomial functions of temperature [105]. Further details and validation of CHT modelling could be found in Ref. [39].

[3]Note the acoustic impedance of the air and fuel lines have been recently verified to have only marginal impact on the thermoacoustic flame dynamics. More information can be found in Ref. [39]

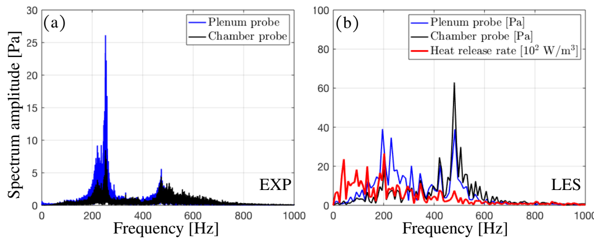

Figure 3: Amplitude of the Discrete Fourier Transform (DFT) of (a) the experimentally measured pressure fluctuations recorded in the plenum (blue) and in the combustion chamber (black) as well as (b) LES predicted signals of heat release rate (red), pressure in the plenum (blue) and in the combustion chamber (black). Case *A*: 0% H_2 [39].

3. Experimental measurements and LES predictions

Numerical and experimental data acquired for Cases *A* (section 3.1), *B* (section 3.2) and *C* (section 3.3) are hereafter presented.

3.1. Case A: pure CH_4 flame

Figure 3(a) presents the amplitude of the Discrete Fourier Transform (DFT) of the experimentally measured pressure fluctuations recorded in the plenum (blue) and in the combustion chamber (black). The combustion chamber microphone probe is mounted in the corner post, 20 mm downstream of the backplane of the burner (as the LES probe). No thermoacoustic activity is observed for this operating condition. The spectrum is characterized by two modes, at 260 Hz and 480 Hz, with peak amplitudes smaller than 10 Pa (in the combustion chamber). In agreement with experiments, LES predicts a stable flame (Fig. 3(b)) where limited

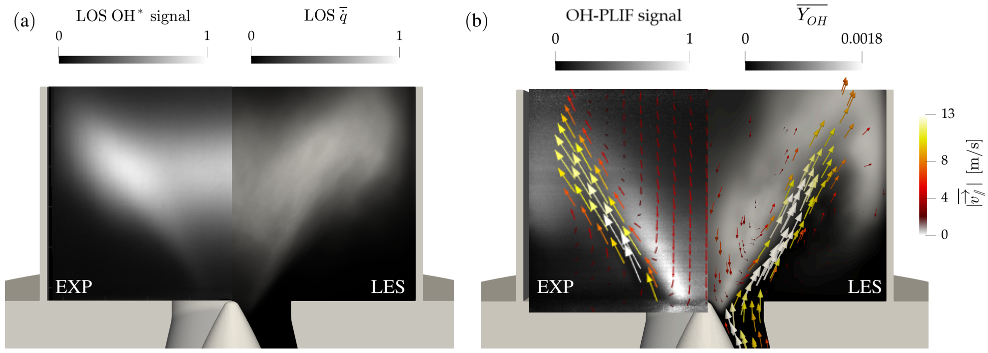

Figure 4: (a) Comparison of experimentally measured normalized time-averaged Line of Sight (LOS) OH* chemiluminescence image with LOS predicted heat release rate $\bar{q}$. (b) Comparison of experimentally measured normalized time-averaged OH-PLIF signal with predicted OH mass fraction $\overline{Y_{OH}}$. The arrows show the component of the time averaged velocity field in the plane $\overrightarrow{v_{//}}$. Case *A*: 0% H_2 [39].

correlation is observable between pressure and heat release rate fluctuations [4].

A visualization of the flame shape is presented in Fig. 4. The normalized time-averaged LOS OH* chemiluminescence image and LOS field of the numerically predicted heat release rate $\bar{q}$ are presented in Fig. 4(a) and show the LES to predict the correct flame length and angle. A region of high heat release rate is predicted in the top central part of the flame while low intensity is predicted in the Central Recirculation Zone (CRZ), just downstream of the centerbody. The flame tip shape and the distance from the external chamber walls are also well recreated. Comparison of the normalized time-averaged OH-PLIF signal with the predicted OH mass fraction is shown in Fig. 4(b). The measured and computed time-averaged velocity fields in the plane $\overrightarrow{v_{//}}$ are indicated by arrows that are tangential to the velocity vector and whose length and color indicate the velocity magnitude. Both in experiments and LES, a high velocity region (i.e. white arrows) is present at the swirler exit. The CRZ is indicated by the downward velocity vectors while in the Outer Recirculation Zone (ORZ) the velocity component in the plane is very weak [39].

3.2. *Case* B*: 20%* H_2 *enrichment*

Figure 5(a) presents the pressure fluctuations recorded for Case *B* (20% H_2) in the plenum (blue) and in the combustion chamber (black) as well as the volume-integrated OH* chemiluminescence signal (red). The pressure signal shows fluctuation levels of 400 Pa in the plenum, while the amplitude in the combustion chamber is close to 200 Pa. The fluctuations

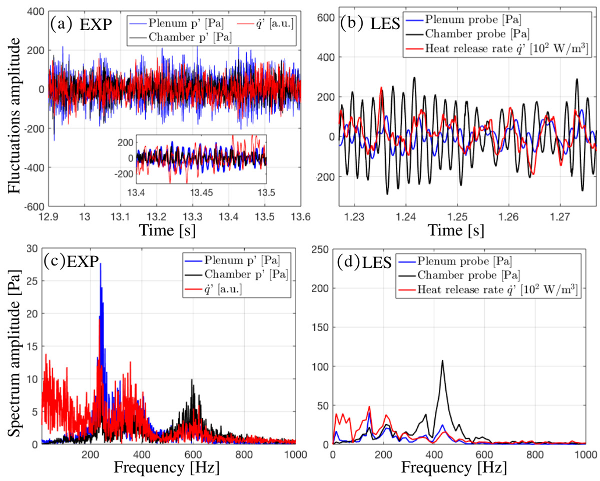

Figure 5: (a) Experimentally measured and (b) LES predicted fluctuations of pressure in the plenum (blue) and in the combustion chamber (black). The red line reports (a) volume-integrated OH* chemiluminescence signal and (b) heat release rate. (c-d) Signals DFT amplitude. Case *B*: 20% H_2.

of the volume-integrated OH* chemiluminescence signal (red) appear not to be strongly correlated to the pressure fluctuations. Similarly to Case *A*, only small peaks appear in the DFT (Fig. 5(c)), confirming that no strong self-excited pulsation takes place although levels reached are higher than Case *A*. The time-series (computed via LES) of the heat release rate (red) and pressure signal in the plenum (blue) as well as at the combustion chamber backplane (black) are presented in Fig. 5(b). The (numerically) computed pressure fluctuation amplitude in the chamber and in the plenum is of the order of 400 Pa and corresponds to the level observed experimentally (Fig. 5(a)). Like in the experimental data, heat release rate fluctuations do not appear to be strongly cor-

[4] Note that this pure CH_4 flame was extensively investigated in a previous work of the same authors and a detailed validation and analysis of numerical predictions can be found in Ref. [39].

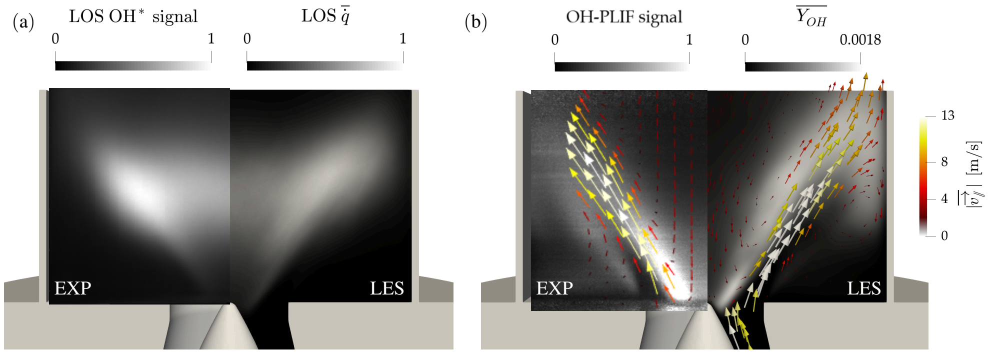

Figure 6: Case B: 20% H_2. Comparison experiments/LES (a-b) labelled as in Fig. 4.

related with pressure fluctuations as confirmed by the corresponding DFT presented in Fig. 5(d). Numerically, a stronger peak is predicted for the chamber pressure at 430 Hz [5] but it appears to be not correlated with heat release rate fluctuations, leading to the conclusion that the 20% H_2-enrichment does not lead to significant differences in the flame dynamics when compared to the pure CH_4 case. At most, this case produces more noise.

Figure 6(a) compares the normalized time-averaged LOS OH* chemiluminescence image with LOS of the numerically predicted heat release rate $\bar{\dot{q}}$. The flame is shorter compared to the pure CH_4 case (Fig. 4(a)) and presents a higher signal intensity region in the central part while no flame is observed downstream the centerbody tip. For both cases, LES accurately predicts the flame shape, i.e. flame angle and length. Figure 6(b) compares the normalized time-averaged OH-PLIF signal with the OH mass fraction predicted via LES on a vertical plane. The flame has a V-shape with the high OH concentration close to the centerbody tip. Low OH concentration is present in the ORZs and in the CRZ just downstream of the centerbody tip, where a high velocity region is present at the injector exit. Overall, LES is able to accurately predict the experimentally measured velocity field (quantitative comparison is left to the Appendix A).

3.3. *Case* C*: 50%* H_2*-enrichment*

Figure 7(a) presents the pressure fluctuations recorded in the plenum (blue) and in the combustion chamber (black), together with the fluctuations of the volume-integrated OH* chemiluminescence signal (red). The pressure oscillations are notably higher than

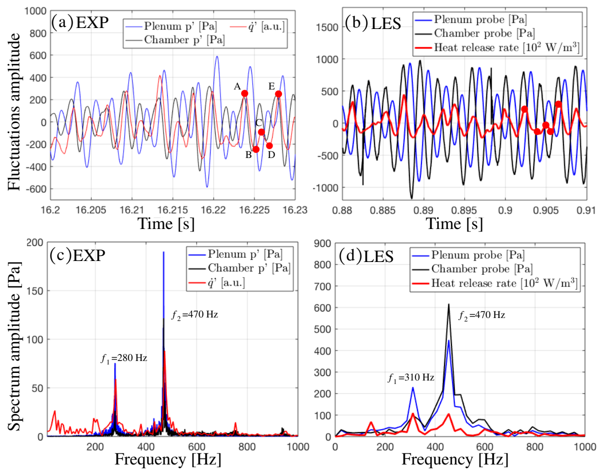

Figure 7: Case C: 50% H_2. (a-b) Signals and (c-d) spectra as labelled in Fig. 5.

those of Cases A and B, reaching an amplitude of 1000 Pa and 600 Pa for the plenum and chamber probes respectively. Heat release rate fluctuation appears here to be correlated to the pressure fluctuation, with a phase difference within the $\pi/2$ limit, satisfying the well-known Rayleigh criterion [107]. This hypothesis is confirmed by looking at DFT of the full signals, Fig. 7(c). Both pressure DFT as well as the volume-integrated OH* chemiluminescence DFT show two strong peaks in this case at 280 Hz and 470 Hz. The peak at 470 Hz is significantly stronger, reaching an amplitude of approximately 200 Pa in the plenum, and 130 Pa in the combustion chamber, compared to 80 Pa and 40 Pa, respectively, for the peak at 280Hz. The same peaks are present in the volume-integrated OH* chemiluminescence DFT, showing that the flame responds to the two modes, hence suggesting the presence of a bi-modal thermoacoustic oscillation [108]. Pressure and heat re-

[5]The slight overestimation of DFT amplitude in LES can be linked to the absence of experimental acoustic damping from the combustor side walls [106].

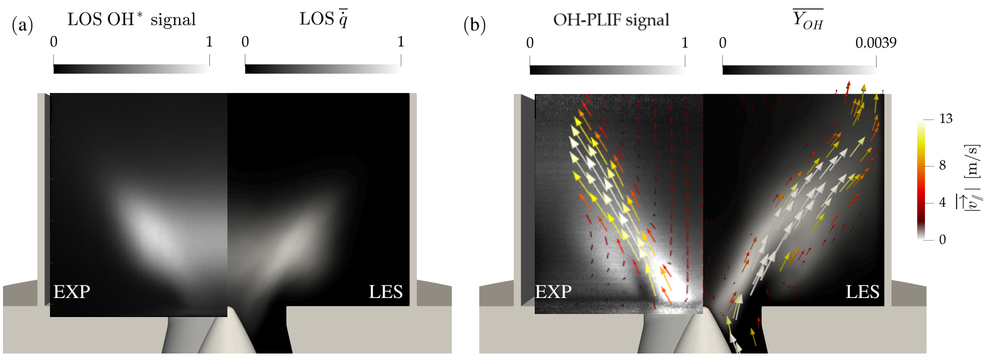

Figure 8: Case C: 50% H_2. Comparison experiments/LES (a-b) labelled as in Fig. 4.

lease rate oscillations computed via LES are shown in Fig. 7(b). A first weak peak at 310 Hz (which is close to the experimental value of 280 Hz) and a stronger one matching the experimental frequency of 470 Hz are clearly retrieved in both pressure and heat release rate DFT, Fig. 7(d).

Figure 8(a) compares the (LOS-integrated) OH* chemiluminescence measured experimentally and the heat release rate $\bar{q}$ predicted via LES. In the Case C the flame is more compact and stabilizes further upstream than do those of Cases A and B. The LES accurately predicts the flame shape but slightly under-estimates the flame length. A more detailed comparison is performed in Fig. 8(b), showing the normalized time-averaged OH-PLIF signal and the numerically-predicted OH mass fraction $\overline{Y_{OH}}$ [6]. In both experiments and LES, the OH field is more compact compared to Cases A and B. This reduction in length is however less evident if compared to the decrease in flame length observed from the heat release rate field. For example, OH values almost reach the lateral chamber walls while the heat release rate does not. This is not unexpected, as the OH radical has a very long lifetime compared to that of the heat-release reactions. Therefore, OH persists in the burned gases long after the heat-release reactions are complete. Note also that the peak value of the OH mass fraction is more than doubled compared to the other cases and the highest value is clearly reached just downstream of the centerbody tip [23]. The presence of OH in the ORZ implies high temperatures in these regions, as OH signal is usually observed in high temperature, post-combustion gases. The acceleration of the flow due to the increased combustion intensity is visible from the velocity vectors that are tangential to the experimental and numerical time-averaged velocity field in the plane $\overrightarrow{v_{//}}$ (their length and color indicate the velocity magnitude). LES accurately predict the experimental velocity field (quantitative comparison proposed in Appendix A) and no OH is detected in the high velocity region at the injector exit.

The experimentally observed and numerically predicted flame dynamics are visualized in Fig. 9. Instantaneous fields of (top) experimental normalized time-averaged OH-PLIF signal are compared to LES-predicted (middle) OH mass Y_{OH} and (bottom) fields of hydrogen mass fraction Y_{H_2} (left) along with the flow vorticity normal to the plane $\omega_\perp$ (right) with superimposed heat release rate $\dot{q}$. Five equivalent instants for experiments and LES are considered as depicted in Fig. 7(a-b). Instants (a) and (e) correspond to two large consecutive peaks in the volume-integrated OH* chemiluminescence signal and the predicted heat release rate. Instants (b) and (d) correspond to two minima while instant (c) corresponds to a small intermediate peak of the signals. In both experiments and LES, flame dynamics is observed to be characterized by four periodic interacting phenomena:

- the change in flame length and flame surface, maximum at instants (a), (c) and (e) when the predicted heat release rate and OH* chemiluminescence signal present high values;
- the stabilization point of the flame roots that moves upstream, as at instant (c), or downstream, as at instant (b), along the centerbody walls;
- the flapping of the jet fuel causes rich gas pockets that are released in the combustion chamber[7],

[6] Note that the OH-PLIF signal is not a direct measure of OH number density since there are a number of factors that can affect OH-PLIF signal intensity, including pressure, quenching, laser and signal absorption. However OH-PLIF signal can be considered as proportional to OH mass fraction as a first approximation.

[7] Note that local equivalence ratio fluctuations have been previ-

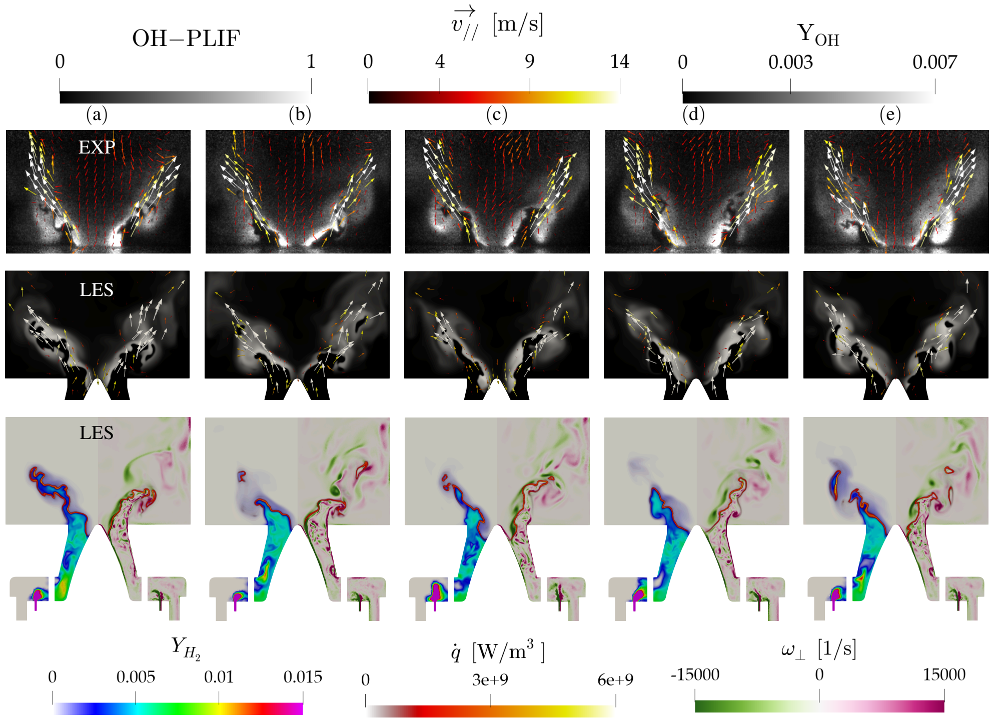

Figure 9: Instantaneous fields during the bi-modal dynamics for experiments and LES, Case C: 50% H_2. Normalized OH-PLIF signal (top), LES-predicted OH mass Y_{OH} (middle) and hydrogen mass fraction Y_{H_2} (left, bottom) and flow vorticity normal to the plane $\omega_\perp$ (right, bottom) with superimposed the heat release rate $\dot{q}$.

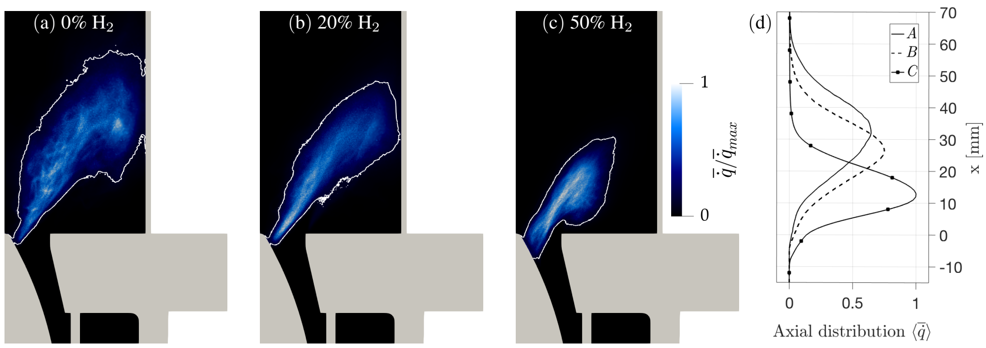

Figure 10: Normalized time-averaged heat release rate $\bar{\dot{q}}/\bar{\dot{q}}_{max}$ predicted by CHT simulations for Cases (a) A, (b) B and (c) C. White isocontours indicate 10% of $\bar{\dot{q}}_{max}$. (d) Corresponding normalized axial distributions of time-averaged heat release rate $\langle\bar{\dot{q}}\rangle$.

as visible for example from the non-homogenous hydrogen mass fraction field near the backplane at instant (c);

- the vortical structures detaching from the center-body tip and the backplane interacting with the flame front yielding wrinkling and flame roll-up, as for example indicated by the region of high OH-PLIF signal near the backplane at instant (e).

ously observed in many experimental and numerical studies on PRECCINSTA operated with CH_4 when the first acoustic mode of the system is excited, e.g. Refs [68, 39, 73]. Indeed, in this case, the velocity field at the exit of the fuel injector oscillates leading to fuel accumulation (rapid release) when the velocity is low (high). This in turn causes rich gas pockets to be periodically pushed into the chamber causing heat release oscillations which sustain the thermoacoustic limit cycle.

4. H_2-enrichment effects

The effects of H_2-enrichment on the flame shape and stabilization (section 4.1), thermal load and temperature fields (section 4.2) as well as the flame dynamics (section 4.3) are hereafter analyzed.

4.1. Flame shape and stabilization

Comparison of the mean flame shapes as predicted by CHT simulations is at first discussed. To do so, Fig. 10 first presents the normalized time-averaged heat release $\bar{q}/\bar{q}_{max}$ for Cases (a) A, (b) B and (c) C. Case A and B show a V shape flame, with the flame root stabilized at the centerbody tip. The 20% H_2-enrichment yields a slightly reduced flame length and a larger flame angle. This is linked to to the higher expansion of the burnt gases in the CRZ caused by the more intense heat release rate. When 50% H_2-enrichment is considered (c), the flame gets even shorter and becomes more compact [109]. It is also stabilized more upstream along the centerbody presenting a quasi M-flame shape [26, 110] with a reduced lift-off distance from the combustion chamber backplane. Note that Case C presents a blurry flame root near the centerbody tip, indicating that the flame stabilization point moves in time during the thermoacoustic oscillation.

To obtain a more quantitative comparison between the three flames in terms of shape and stabilization, the time-averaged heat release rate is integrated over the combustor cross section S_c to yield the one-dimensional mean axial distribution $\langle\bar{q}\rangle$, as expressed by

$$\langle\bar{q}\rangle(x) = \frac{1}{S_c}\iint_{S_c} \bar{q}(x, y, z)dydz. \qquad (1)$$

The resulting axial distributions of time-averaged heat release rate $\langle\bar{q}\rangle$ are then normalized by the maximum value of the Case C and are presented in Fig. 10(d). Case A clearly presents the most spread out axial distribution, with a maximum heat release rate located around x=35 mm from the backplane and a weak heat release rate at the centerbody tip axial location (i.e. x=0 mm). In Case B, the flame becomes slightly shorter and shifts upstream, with a higher maximum of heat release rate located near 25 mm downstream of the backplane. The flame root position however does not differ significantly from Case A aside from having a higher heat release rate. Finally, Case C shows a more compact flame which is shifted further upstream with a clear maximum value at 14 mm from the backplane. The mean stabilization location of the flame root moves 10 mm upstream inside the injector.

4.2. Thermal load and fluid temperature

Instantaneous solid temperature fields computed via numerical simulation are shown in Fig. 11 for Cases (a) A, (b) B and (c) C along with the instantaneous iso-contours of heat-release rate $\dot{q}$ at 10% of $\dot{q}_{max}$. This latter clearly shows the reduction in flame length and the change in flame root stabilization position due to hydrogen enrichment. As expected, the three flame structures lead to differences in the solid wall temperatures. The temperature profiles along the internal side of the combustion chamber walls (Fig. 11(e), red line in Fig. 11(d)), are very similar for the three flames. For Case A, the temperature of the chamber walls on the internal side reaches a maximum value of 1300 K 40 mm from the backplane where the flame is close to the walls while, for Case B and C, the maximum temperature is 50 K lower (1250 K) probably due to the larger distance between the flame and this chamber wall. Contrarily, the temperature field at the centerbody tip (Figure 11(f), blue line in Fig. 11(d), differs significantly. Case C exhibits higher centerbody tip temperature (1200 K) than cases A (1000 K) and B (850 K), suggesting that H_2 addition leads to significantly larger heat loads on the burner. Finally, the profiles plotted in Fig. 11(g) (green line in Fig. 11(d)) show surface temperature at the combustor backplane increase with increasing hydrogen admixture. This is likely due to the previously noted decrease in flame lift-off distance with increasing hydrogen content in the fuel. This increase is, however, relatively minor compared to the temperature increase at the centerbody tip.

Figure 12 presents the time-averaged temperature $\overline{T}$ in a cut plane for Cases (a) A, (b) B and (c) C (the fluid domain is delimited by a white line). For Cases A and B, the flow reaches 1800 K in the CRZ and downstream of the flame tip where burnt gases are present while ORZs present lower temperature levels. Indeed, compared to Case A, although H_2 is added the adiabatic flame temperature of Case B is only slightly higher, leading to a quite similar fluid temperature $\overline{T}$. In contrast, for Case C, which has much more H_2, the combustion chamber contains more hot burnt gases. In all cases, the red iso-contours correspond to a temperature of 450 K and show the pre-heating of the fresh gases due to the heated solid. As expected due to the higher centerbody tip temperature, pre-heating of the fresh gases occurs consistently more upstream when increasing the hydrogen content for Cases B and C respectively.

4.3. Flame dynamics: bi-modal oscillation analysis

The nature of the two main components of the observed bi-modal oscillations are at first investigated computing the system acoustic modes using the AVSP

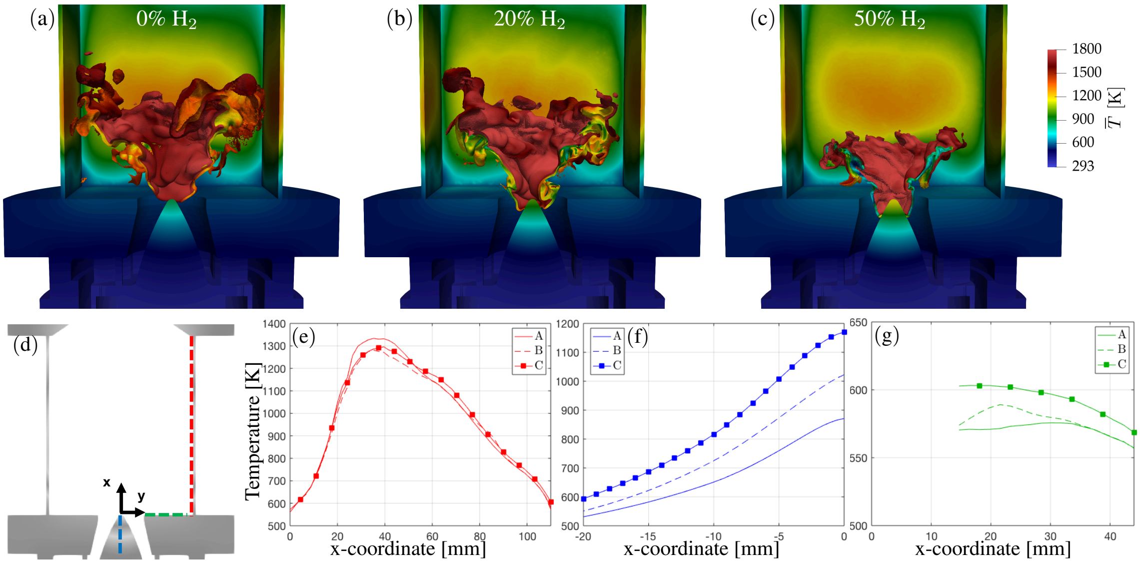

Figure 11: Comparison of CHT-predicted instantaneous field of solid temperature with iso-contour of heat-release rate $\dot{q}$ at 10% of its maximum value for Cases (a) *A*, (b) *B* and (c) *C*. (d) Schematic of the test bench with location of the profiles. Temperature profiles (e) along the internal side of the combustion chamber walls, (f) through the centerbody and (g) at the backplane.

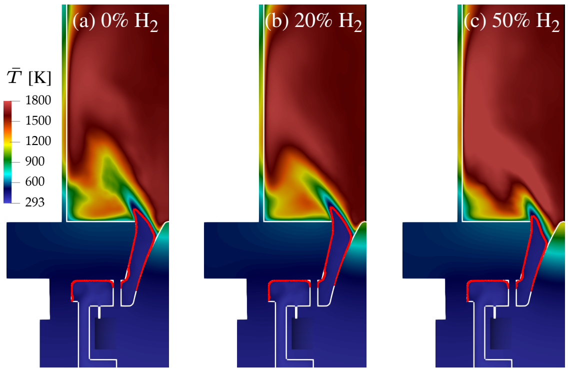

Figure 12: Cut-plane showing the predicted time-averaged temperature $\overline{T}$ for Cases (a) *A*, (b) *B* and (c) *C*. Red iso-contour corresponds to temperature of 450 K. The fluid domain is delimited by a white line to visualize the separation between solid and the fluid parts.

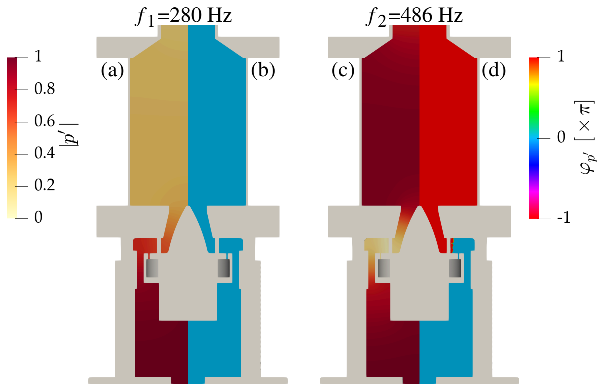

Figure 13: Acoustic modes computed with the Helmholtz solver. (a) Amplitude and (b) phase of the first acoustic (plenum) mode at 280 Hz. (c) Amplitude and (d) phase of the second acoustic (chamber) mode at 486 Hz. Case *C*: 50% H_2.

Helmholtz solver [111][8]. Regardless of the presence of hydrogen, results show no significant differences in the frequency of the first modes for the three cases, suggesting that variations in the flow mean temperature distributions previously discussed (Fig. 12) are not sufficient to change system acoustics significantly.Two acoustic modes are found at frequencies close to the two peaks recorded in pressure and heat release rate signals of Case *C*. The first mode predicted at 280 Hz (Fig. 13(a-b)) is the 1/4 wave (or bulk) mode of the system: the amplitude of the pressure oscillation $|p'|$ is larger in the plenum (Fig. 13(a)) and both the combustion chamber as well as the plenum oscillate in phase (Fig. 13(b)). Note that this first acoustic mode is the one that is generally excited when dealing with unstable pure methane flames during limit cycle oscillations in the PRECCINSTA burner, as for example in the work of Meier *et al.* [68]. The second acoustic mode at 486 Hz (Fig. 7) corresponds to a 3/4 wave (chamber) mode: a pressure antinode is found in the combustion chamber and both

[8]Note that, in the Helmholtz solver, a velocity node has been imposed for the air and fuel inlets, while a pressure node has been imposed at the combustion chamber outlet as acoustic boundary conditions.

the combustion chamber as well as the plenum oscillate in phase opposition. Note that this specific feature is reported in both the experiments and LES. The amplitude of the chamber oscillations are however not-constant and lower than the plenum ones due to the combination of the second mode with the first acoustic mode oscillations at 280 Hz (Fig. 7(a)). The specific coupling of the flame with this second mode has not been observed for classical pure methane flames and it is likely due to hydrogen enrichment.

The impact of hydrogen enrichment on the flame dynamics is hereafter investigated. To this scope, Dynamic Mode Decomposition (DMD) [112] is used to reconstruct the oscillating modes of the system and extract the response of the variables of interest at a certain frequency [113]. For the present study, since the 50% H_2-enriched case presents a bi-modal thermoacoustic oscillation, the frequencies of interest are selected at the first f_1 (280 Hz)[9] and at the second f_2 (470 Hz) acoustic modes of the system. To do so, DMD of the experimental OH-PLIF signal and the LES data for pressure (p), heat release rate ($\dot{q}$), flow vorticity normal to the plane ($\omega_\perp$), OH mass fraction (Y_{OH}) and H_2 mass fraction (Y_{H_2}) are computed. DMD input for the experimental data is 1000 OH-PLIF images while, for the simulations, the input is 1000 instantaneous 3D LES fields (i.e. 100 ms physical time).

Figure 14 presents a cut-plane showing the DMD mode at f_1 = 280 Hz (top) and f_2 = 470 Hz (bottom). First, the normalized real part for the (a-f) experimental OH-PLIF signal is compared to (b-g) the predicted OH mass fraction through $\mathcal{R}e(\widehat{Y_{OH}})$. LES is able to accurately reproduce the DMD spatial distribution of experimental OH-PLIF signal for both modes, suggesting the correct reproduction of the flame dynamics.

The spatial distribution of the Rayleigh index, Fig. 14(c-h), $\mathcal{R}e(\widehat{RI}) = \mathcal{T}_{q,p} = |\hat{p}||\hat{q}|\cos\left(\varphi_q - \varphi_p\right)$, reveals regions contributing to the enhancement or damping of the instabilities [114, 115]. As expected during a self-sustained thermoacoustic oscillation, large regions of positive heat release rate/pressure coupling (red zones) are observed for the two modes. Figure 14(d-i) shows as a complement the H_2 mass fraction - pressure fluctuation correlation index, $\mathcal{T}_{Y_{H_2},p} = |\hat{p}||\hat{Y_{H_2}}|\cos\left(\varphi_{Y_{H_2}} - \varphi_p\right)$. As for the Rayleigh index, large zones of positive coupling, i.e. where jet flapping induced equivalence ratio oscillations are in phase with the pressure fluctuation, happen for the two frequencies. Likewise, the vorticity - pressure fluctuation correlation index (Fig. 14(e-l)), $\mathcal{T}_{\omega_\perp,p} = |\hat{p}||\hat{\omega_\perp}|\cos\left(\varphi_{\omega_\perp} - \varphi_p\right)$, indicates whether fluctuations of flow vorticity $\omega_\perp$ are contributing positively or negatively to the pressure oscillations. Differently from the two previous indices, a coherent distribution appears only for the f_2 DMD mode. Indeed, at this frequency, a vortex seems to first detach from the backplane when pressure is decreasing (blue region just at the backplane corner) and then it is convected downstream (purple region) interacting with the flame front and positively contributing to the instability, i.e. the purple region corresponds to the red positive Rayleigh index region in Fig. 14(h). The vortex convection time can be easily estimated dividing the distance between the backplane and the point of highest vorticity ($\approx$ 14 mm, see black arrow) by the mean velocity ($\approx$ 13 m/s) resulting in 1.07 ms, which corresponds to half the period of the second acoustic mode at 470 Hz. This characteristic time is not synchronised with f_1, explaining the uncorrelated field for this mode. The flame/vortex coupling at f_2 likely drives or plays a role for the second of the two modes, characterising the thermoacoustic instabilities observed in this case. Note that the zone of highest vorticity corresponds to the region where heat release rate fluctuation results in the largest contribution to the pressure oscillation, i.e. positive red Rayleigh index region in Fig. 14(h) and periodic flame roll-up is observed both in experiments and LES, Fig. 9.

Based on the last specific analysis, the impact of hydrogen enrichment on the flame dynamics is understood to be as follows. By increasing H_2 content, a reduction in the flame length and a transition towards a M-shape flame (Fig. 10) modify the flame response to acoustic oscillations [110, 116]. Instabilities coupled with the first acoustic mode of the system are supported by equivalence ratio oscillations associated with the jet flapping as usually reported for this configuration. Differently from the methane cases, a second acoustic mode is excited at 50% of hydrogen enrichment. The onset of this bi-modal oscillation is explained by modifications of the interactions between the flame front and vortices shaded at the backplane corner. When the flame length is reduced, the convection time of the vortices needed to reach the heat release rate mean region synchronizes to exactly half the period of the system second acoustic mode, explaining the observed bi-modal response.

[9]Note that, since numerically the oscillations at the first mode correspond to a frequency slightly higher (i.e. 310 Hz), clearly the latter is used for extracting the DMD from LES data.

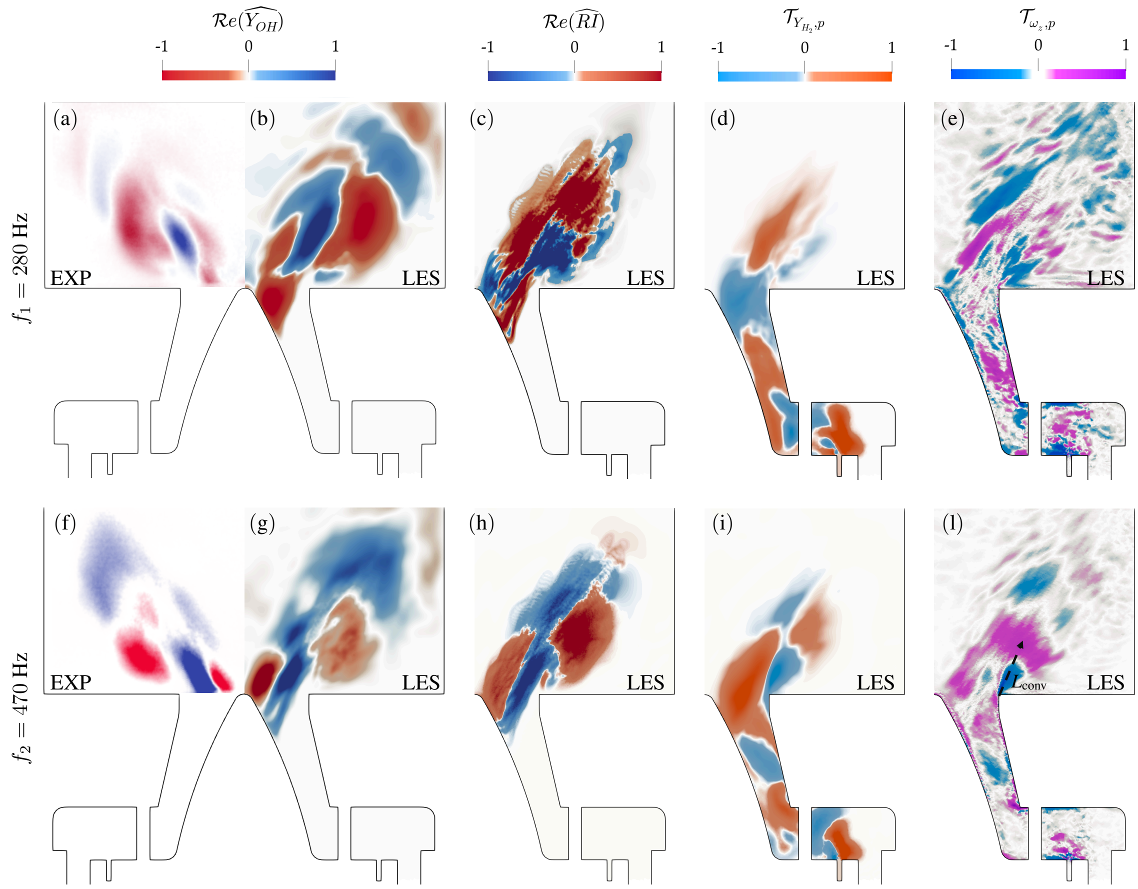

Figure 14: Cut-plane showing the Dynamic Mode Decomposition (DMD) at 280 Hz (top) and 470 Hz (bottom). Normalized real part of the (a-f) experimental OH-PLIF signal and the (b-g) LES-predicted OH mass fraction in frequency domain $\mathcal{R}e(\widehat{Y_{OH}})$. Normalized real part of the LES (c-h) Rayleigh index $\mathcal{R}e(\widehat{RI})$, (d-i) H_2 mass fraction - pressure fluctuations correlation index $\mathcal{T}_{Y_{H_2},p}$ and (e-l) flow vorticity - pressure fluctuations correlation index $\mathcal{T}_{\omega_\perp,p}$. Case C: 50% H_2.

5. Conclusions

The impact of H_2-enrichment on flame stabilization and combustion dynamics of a CH_4 lean partially-premixed turbulent swirling flame is studied both experimentally and by LES. To do so, the well-known PRECCINSTA burner is operated with increasing levels of hydrogen enrichment while acquiring synchronized OH-PLIF imaging, sPIV velocity fields data, LOS OH* chemiluminescence images and pressure signal recordings. Numerically, LES simulations are performed in the Conjugate Heat Transfer (CHT) context for three flames operating with different hydrogen enrichment levels: the pure methane flame A, the 20% H_2-enriched flame B and the 50% H_2-enriched flame C. LES results are first validated against experimental data in terms of predicted velocity fields, heat release rate distribution, OH mass fraction and pressure signals in the combustion chamber and in the plenum, all quantities providing satisfactory agreement.

Hydrogen addition results in modifications of the flame shape and stabilization, the temperature field and the flame dynamics. The 20% H_2-enriched flame B presents a more compact heat release rate distribution when compared to the pure methane flame A: the flame is slightly shorter due to the increase in laminar flame speed while the higher adiabatic flame temperature together with the more upstream flame root stabilization lead to a notably higher centerbody tip temperature. However, both flames A and B present no significant thermoacoustic oscillation and show relatively low pressure and heat release rate fluctuations. Contrarily, when considering the 50% H_2-enriched case C, the flame has a notably more compact heat release rate distribution and a shorter length due to the significant increase in laminar flame speed. In addition, CHT results show that, while the chamber walls and the backplane surface temperatures are only marginally affected, the centerbody tip reaches a notably higher temperature compared to flames *A* and *B*. At the same time, the flame dynamics drastically changes: significant thermoacoustic oscillation is observed both experimentally and numerically. The flame couples both with the first and second system acoustic modes, showing bi-modal thermoacoustic oscillation.

Flame dynamics of Case *C* are further analyzed by comparing equivalent instants of experimental OH-PLIF images to OH mass fraction computed via LES. Four periodic phenomena are identified supporting the bi-modal oscillation: the change in flame length and flame surface, the stabilization point of the flame root that moves upstream/downstream along the centerbody walls, the flapping of the jet fuel causing rich gas pockets to be released in the combustion chamber and finally the vortical structures shedding from the centerbody tip and the backplane that then interact with the flame front leading to strong wrinkling and flame roll-up. Further insights on these phenomena are investigated by Dynamic Mode Decomposition (DMD) analysis of both OH-PLIF images and LES 3D fields at the system first and second acoustic modes. It is shown that a coupling of vortical structures with thermoacoustic modes are observed only for the second acoustic mode.

Therefore, H_2-enrichment of the PRECCINSTA partially-premixed methane swirling flame is shown to affect the flame shape and length as well as its stabilization. These modifications are likely the key elements leading to the onset of the observed bi-modal thermoacoustic instability. The Flame Transfer Function (FTF) [117] of such flames would be required to further confirm this hypothesis. However, no experimental measurements of these FTFs are currently available, their numerical calculations being also out of the scope of the present study. Nevertheless, for all considered H_2-enrichment cases, the proposed LES proved to be able to successfully predict the complex flame dynamics in the CHT context, providing also interesting insights about the hydrogen addition impact on the test rig component temperature.

Acknowledgements and Fundings

This project has received funding from the H2020-MSC-ITN Grant Agreement No 766264 (MAGISTER), the MSCA Grant Agreement No 843958 (CLEANER-FLAMES - D. Laera Individual Fellowship), the H2020 Grant Agreement 952181 (COEC - Center of Excellence in Combustion) and the ERC H2020 Grant Agreement 832248 (SCIROCCO) and 682383 (HyBurn). HPC resources from the PRACE Projects 2020225434 (FANTASTIC-H2) and 2020225436 (REVOLUTION) are also acknowledged. The authors would also like to thank Dr. Stephane Richard from Safran Helicopter Engines (SHE) for valuable discussions and Dr. Florent Duchaine from CERFACS for support on the AVTP solver.

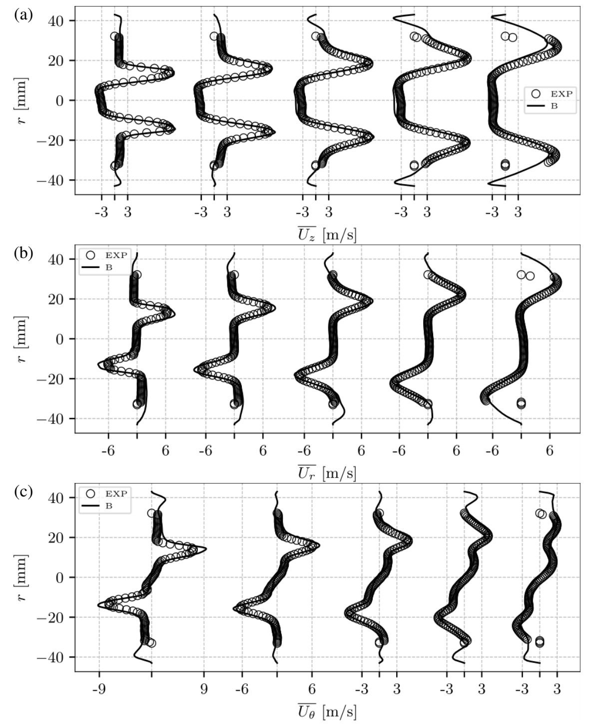

Figure A.15: Profiles of mean (a) axial, (b) radial and (c) tangential velocity components at measurement planes at x = 6, 10, 15, 20 and 30 mm downstream of the combustion chamber backplane for LES in comparison to experiments. Case *B*: 20% H_2.

Appendix A. Validation of LES predicted velocity fields

Quantitative validation of velocity field predicted via LES is provided in this Appendix for Cases *B* and *C*. Note that LES validation of Case *A* can be found in Ref. [39].

Figure A.15 and Fig. A.16 presents, respectively, the profiles of mean and RMS (a) axial, (b) radial and (c) tangential velocity components at different distances downstream of the combustion chamber backplane for LES and from to sPIV for Case *B*. The mean axial velocity (a) shows an extended CRZ, indicated by the negative velocity values. The mean (b) radial and (c) tangential velocity components are also well predicted by

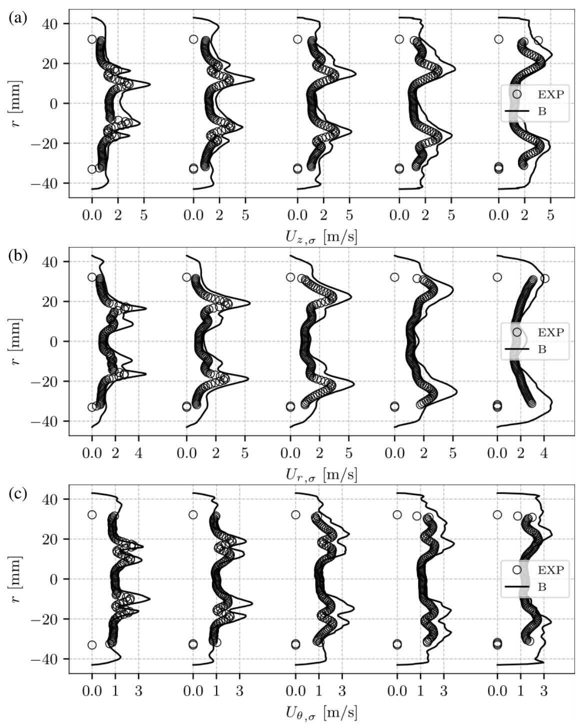

Figure A.16: Case B: 20% H_2. Profiles of RMS : (a-c) labelled as in Fig. A.15

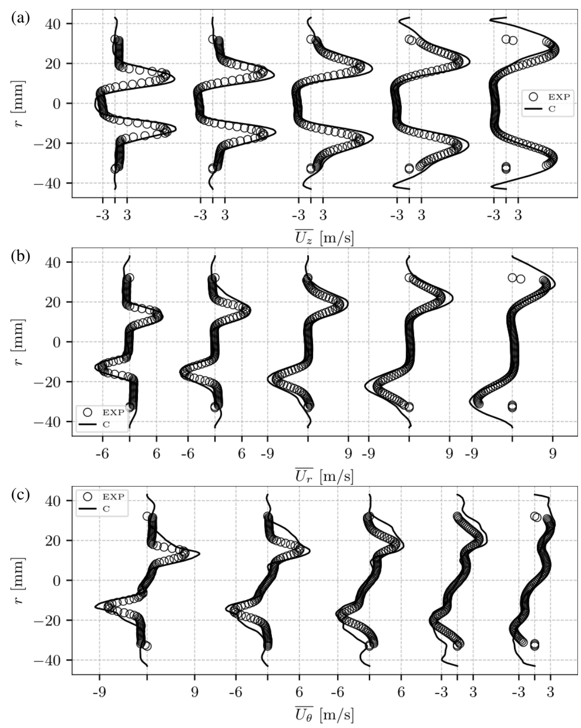

Figure A.17: Profiles of mean (a) axial, (b) radial and (c) tangential velocity components at measurement planes at x = 6, 10, 15, 20 and 30 mm downstream of the combustion chamber backplane for LES in comparison to experiments. Case C: 50% H_2

LES. In terms of RMS, considering the low velocity magnitude, LES shows satisfactory agreement with experimental values. Indeed, the slight overestimation of the peaks visible on the three components can be explained by taking into account experimental uncertainties. Note that the most significant discrepancy between LES and experiments happens for the tangential component of velocity: this poorer match is not unexpected as in sPIV it is well established that measurement uncertainty in the out-of-plane direction (in this case, the tangential) is typically higher than for the in-plane components of velocity [118].

Validation of the velocity field for Case C is performed in Fig. A.17 and Fig. A.18 by comparing, respectively, the LES profiles of mean and RMS (a) axial, (b) radial and (c) tangential velocity components with the experimental data at different measurement planes downstream of the combustion chamber backplane. The mean axial velocity component, Fig. A.17(a), shows an extended CRZ whose magnitude is well captured by LES. The latter is able to predict the correct opening of the jet (i.e. flame angle) as already observed from the flame shape validation. The mean radial, Fig. A.17(b), and tangential velocity, Fig. A.17(c), component LES profiles show satisfactory agreement with the experimental data, in terms of jet opening and magnitude. When it comes to RMS velocity components (Fig. A.18), the LES slight overestimation can be attributed again to the uncertainty of the experimental data and to the slightly larger pressure levels oscillations predicted by LES.

References

[1] H. Yilmaz, O. Cam, I. Yilmaz, Experimental investigation of flame instability in a premixed combustor, Fuel 262 (2020) 116594.

[2] G. Zang, J. Zhang, J. Jia, E. S. Lora, A. Ratner, Life cycle assessment of power-generation systems based on biomass integrated gasification combined cycles, Renew. Energy 149 (2020) 336–346.

[3] P. S. P. Corrêa, J. Zhang, E. E. S. Lora, R. V. Andrade, L. R. de Mello e Pinto, A. Ratner, Experimental study on applying biomass-derived syngas in a microturbine, Appl. Therm. Eng. 146 (2019) 328–337.

[4] R. K. Cheng, D. Littlejohn, W. A. Nazeer, K. O. Smith, Laboratory studies of the flow field characteristics of low-swirl injectors for adaptation to fuel-flexible turbines, J. Eng. Gas Turbines Power 130 (2008) 021501.

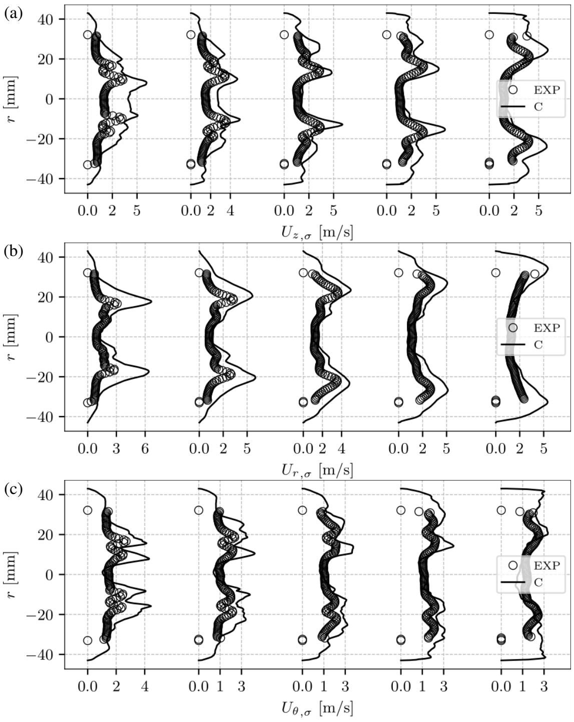

Figure A.18: Case C: 50% H_2. Profiles of RMS : (a-c) labelled as in Fig. A.17

[5] M. C. Lee, J. Yoon, S. Joo, Y. Yoon, Gas turbine combustion characteristics of H2/CO synthetic gas for coal integrated gasification combined cycle applications, Int. J. Hydrog. Energy 40 (2015) 11032–11045.

[6] S. Taamallah, K. Vogiatzaki, F. Alzahrani, E. Mokheimer, M. Habib, A. Ghoniem, Fuel flexibility, stability and emissions in premixed hydrogen-rich gas turbine combustion: Technology, fundamentals, and numerical simulations, Appl. Energy 154 (2015) 1020–1047.

[7] G. Oztarlik, L. Selle, T. Poinsot, T. Schuller, Suppression of instabilities of swirled premixed flames with minimal secondary hydrogen injection, Combust. Flame 214 (2020) 266–276.

[8] Y. Zhang, J. Wu, S. Ishizuka, Hydrogen addition effect on laminar burning velocity, flame temperature and flame stability of a planar and a curved CH4-H2-air premixed flame, Int. J. Hydrog. Energy 34 (2009) 519–527.

[9] M. Emadi, D. Karkow, T. Salameh, A. Gohil, A. Ratner, Flame structure changes resulting from hydrogen-enrichment and pressurization for low-swirl premixed methane-air flames, Int. J. Hydrog. Energy 37 (2012) 10397–10404.

[10] F. Halter, C. Chauveau, N. Djebaïli-Chaumeix, I. Gökalp, Characterization of the effects of pressure and hydrogen concentration on laminar burning velocities of methane-hydrogen-air mixtures, Proc. Combust. Inst. 30 (2005) 201–208.

[11] D. Ebi, R. Bombach, P. Jansohn, Swirl flame boundary layer flashback at elevated pressure: Modes of propagation and effect of hydrogen addition, Proc. Combust. Inst. 38 (2020) 6345–6353.

[12] R. Ranjan, N. T. Clemens, Insights into flashback-to-flameholding transition of hydrogen-rich stratified swirl flames, Proc. Combust. Inst. 38 (2020) 6289–6297.

[13] I. Chterev, I. Boxx, Effect of hydrogen enrichment on the dynamics of a lean technically premixed elevated pressure flame, Combust. Flame 225 (2021) 149–159.

[14] T. Hussain, M. Talibi, R. Balachandran, Investigating the effect of local addition of hydrogen to acoustically excited ethylene and methane flames, Int. J. Hydrog. Energy 44 (2019) 11168–11184.

[15] S. Barbosa, M. C. De La Garcia, S. Ducruix, B. Labegorre, F. Lacas, Control of combustion instabilities by local injection of hydrogen, Proc. Combust. Inst. 31 (2007) 3207–3214.

[16] T. Lieuwen, V. Yang (Eds.), Combustion instabilities in gas turbine engines: operational experience, fundamental mechanisms and modeling, Progress in astronautics and aeronautics, American Institute of Aeronautics and Astronautics, 2005.

[17] V. Di Sarli, A. D. Benedetto, Laminar burning velocity of hydrogen–methane/air premixed flames, Int. J. Hydrog. Energy 32 (2007) 637–646.

[18] Z. Chen, Effects of hydrogen addition on the propagation of spherical methane/air flames: A computational study, Int. J. Hydrog. Energy 34 (2009) 6558–6567.

[19] T. Boushaki, Y. Dhué, L. Selle, B. Ferret, T. Poinsot, Effects of hydrogen and steam addition on laminar burning velocity of methane-air premixed flame: Experimental and numerical analysis, Int. J. Hydrog. Energy 37 (2012) 9412–9422.

[20] C. Jiménez, D. Michaels, A. F. Ghoniem, Stabilization of ultra-lean hydrogen enriched inverted flames behind a bluff–body and the phenomenon of anomalous blow–off, Combust. Flame 191 (2018) 86–98.

[21] Y. J. Kim, B. J. Lee, H. G. Im, Hydrodynamic and chemical scaling for blow-off dynamics of lean premixed flames stabilized on a meso-scale bluff-body, Proc. Combust. Inst. 37 (2019) 1831–1841.

[22] X. Kang, R. J. Gollan, P. A. Jacobs, A. Veeraragavan, Suppression of instabilities in a premixed methane–air flame in a narrow channel via hydrogen/carbon monoxide addition, Combust. Flame 173 (2016) 266–275.

[23] R. Schefer, D. Wicksall, A. Agrawal, Combustion of hydrogen-enriched methane in a lean premixed swirl-stabilized burner, Proc. Combust. Inst. 29 (2002) 843–851.

[24] F. Cozzi, A. Coghe, Behavior of hydrogen-enriched non-premixed swirled natural gas flames, Int. J. Hydrog. Energy 31 (2006) 669–677.

[25] T. Guiberti, D. Durox, P. Scouflaire, T. Schuller, Impact of heat loss and hydrogen enrichment on the shape of confined swirling flames, Proc. Combust. Inst. 35 (2015) 1385–1392.

[26] S. Shanbhogue, Y. Sanusi, S. Taamallah, M. Habib, E. Mokheimer, A. Ghoniem, Flame macrostructures, combustion instability and extinction strain scaling in swirl-stabilized premixed CH4/H2 combustion, Combust. Flame 163 (2016) 494–507.

[27] R. K. Cheng, D. Littlejohn, P. A. Strakey, T. Sidwell, Laboratory investigations of a low-swirl injector with H2 and CH4 at gas turbine conditions, Proc. Combust. Inst. 32 (2009) 3001–3009.

[28] H. S. Kim, V. K. Arghode, M. B. Linck, A. K. Gupta, Hydrogen addition effects in a confined swirl-stabilized methane-air flame, Int. J. Hydrog. Energy 34 (2009) 1054–1062.

[29] B. Ge, Y. Ji, Z. Zhang, S. Zang, Y. Tian, H. Yu, M. Chen, G. Jiao, D. Zhang, Experiment study on the combustion performance of hydrogen-enriched natural gas in a DLE burner, Int. J. Hydrog. Energy 44 (2019) 14023–14031.

[30] J. Zhang, A. Ratner, Experimental study on the excitation of thermoacoustic instability of hydrogen-methane/air premixed flames under atmospheric and elevated pressure conditions, Int. J. Hydrog. Energy 44 (2019) 21324–21335.

[31] P. Palies, M. Ilak, R. Cheng, Transient and limit cycle combustion dynamics analysis of turbulent premixed swirling flames, J. Fluid Mech. 830 (2017) 681–707.
[32] D. Laera, P. W. Agostinelli, L. Selle, Q. Cazères, G. Oztarlik, T. Schuller, L. Gicquel, T. Poinsot, Stabilization mechanisms of CH4 premixed swirled flame enriched with a non-premixed hydrogen injection, Proc. Combust. Inst. 38 (2021) 6355–6363.
[33] R. Hilbert, F. Tap, H. El-Rabii, D. Thévenin, Impact of detailed chemistry and transport models on turbulent combustion simulations, Prog. Energy Combust. Sci. 30 (2004) 61–117.
[34] Y. Huang, H. G. Sung, S. Y. Hsieh, V. Yang, Large-Eddy Simulation of Combustion Dynamics of Lean-Premixed Swirl-Stabilized Combustor, J. Propuls. Power 19 (2003) 782–794.
[35] P. Benard, G. Lartigue, V. Moureau, R. Mercier, Large-Eddy Simulation of the lean-premixed PRECCINSTA burner with wall heat loss, Proc. Combust. Inst. 37 (2019) 5233–5243.
[36] X. Han, D. Laera, A. S. Morgans, C. J. Sung, X. Hui, Y. Z. Lin, Flame macrostructures and thermoacoustic instabilities in stratified swirling flames, Proc. Combust. Inst. 37 (2019) 5377–5384.
[37] X. Han, D. Laera, D. Yang, C. Zhang, J. Wang, X. Hui, Y. Lin, A. Morgans, C.-J. Sung, Flame interactions in a stratified swirl burner: Flame stabilization, combustion instabilities and beating oscillations, Combust. Flame 212 (2020) 500 – 509.
[38] M. Shahi, J. B. Kok, J. C. Roman Casado, A. K. Pozarlik, Transient heat transfer between a turbulent lean partially premixed flame in limit cycle oscillation and the walls of a can type combustor, Appl. Therm. Eng. 81 (2015) 128–139.
[39] P. W. Agostinelli, D. Laera, I. Boxx, L. Gicquel, T. Poinsot, Impact of wall heat transfer in Large Eddy Simulation of flame dynamics in a swirled combustion chamber, Combust. Flame 234 (2021) 111728.
[40] C. Kraus, L. Selle, T. Poinsot, Coupling heat transfer and large eddy simulation for combustion instability prediction in a swirl burner, Combust. Flame 191 (2018) 239–251.
[41] C. Fureby, Large Eddy Simulation of turbulent reacting flows with conjugate heat transfer and radiative heat transfer, Proc. Combust. Inst. 38 (2021) 3021–3029.
[42] J. Beita, M. Talibi, S. Sadasivuni, R. Balachandran, Thermoacoustic instability considerations for high hydrogen combustion in lean premixed gas turbine combustors: A review, Hydrogen 2 (2021) 33–57.
[43] K. T. Kim, J. G. Lee, H. J. Lee, B. D. Quay, D. A. Santavicca, Characterization of Forced Flame Response of Swirl-Stabilized Turbulent Lean-Premixed Flames in a Gas Turbine Combustor, Journal of Engineering for Gas Turbines and Power 132 (4).
[44] E. Æsøy, J. G. Aguilar, S. Wiseman, M. R. Bothien, N. A. Worth, J. R. Dawson, Scaling and prediction of transfer functions in lean premixed h2/ch4-flames, Combust. Flame 215 (2020) 269–282.
[45] Z. Lim, J. Li, A. S. Morgans, The effect of hydrogen enrichment on the forced response of ch4/h2/air laminar flames, Int. J. Hydrog. Energy 46 (2021) 23943–23953.
[46] S. Marragou, I. Boxx, L. Selle, T. Poinsot, T. Schuller, Measurements of the transfer function of partially premixed swirling flames in the PRECCINSTA gas turbine model combustor, in: Symposium on Thermoacoustics in Combustion: Industry meets Academia (SoTiC 2021).
[47] J. Yoon, S. Joo, J. Kim, M. C. Lee, J. G. Lee, Y. Yoon, Effects of convection time on the high harmonic combustion instability in a partially premixed combustor, Proc. Combust. Inst. 36 (2017) 3753–3761.
[48] J. Peng, Z. Cao, X. Yu, S. Yang, Y. Yu, H. Ren, Y. Ma, S. Zhang, S. Chen, Y. Zhao, Analysis of combustion instability of hydrogen fueled scramjet combustor on high-speed OH-PLIF measurements and dynamic mode decomposition, Int. J. Hydrog. Energy 45 (2020) 13108–13118.
[49] N. A. Baraiya, S. R. Chakravarthy, Effect of syngas composition on high frequency combustion instability in a non-premixed turbulent combustor, Int. J. Hydrog. Energy 44 (2019) 6299–6312.
[50] J. Zhang, A. Ratner, Experimental study of the effects of hydrogen addition on the thermoacoustic instability in a variable-length combustor, Int. J. Hydrog. Energy 46 (2021) 16086–16100.
[51] S. Nakaya, K. Omi, T. Okamoto, Y. Ikeda, C. Zhao, M. Tsue, H. Taguchi, Instability and mode transition analysis of a hydrogen-rich combustion in a model afterburner, Proc. Combust. Inst. 38 (2021) 5933–5942.
[52] D. Kim, S. Joo, Y. Yoon, Effects of fuel line acoustics on the self-excited combustion instability mode transition with hydrogen-enriched laboratory-scale partially premixed combustor, Int. J. Hydrog. Energy 45 (2020) 19956–19964.
[53] J. Strollo, S. Peluso, J. O'Connor, Effect of hydrogen on steady-state and transient combustion instability characteristics, J. Eng. Gas Turbines Power 143 (2021) 071023.
[54] T. Shoji, S. Tachibana, T. Suzuki, Y. Nakazumi, T. Yokomori, A new pattern of flame/flow dynamics for lean-premixed, low-swirl hydrogen turbulent jet flames under thermoacoustic instability, Proc. Combust. Inst. 38 (2021) 2835–2843.
[55] T. Indlekofer, B. Ahn, Y. H. Kwah, S. Wiseman, M. Mazur, J. R. Dawson, N. A. Worth, The effect of hydrogen addition on the amplitude and harmonic response of azimuthal instabilities in a pressurized annular combustor, Combust. Flame 228 (2021) 375–387.
[56] T. Indlekofer, A. Faure-Beaulieu, N. Noiray, J. Dawson, The effect of dynamic operating conditions on the thermoacoustic response of hydrogen rich flames in an annular combustor, Combust. Flame 223 (2021) 284–294.
[57] J. Nam, J. J. Yoh, A numerical investigation of the effects of hydrogen addition on combustion instability inside a partially-premixed swirl combustor, Appl. Therm. Eng. 176 (2020) 115478.
[58] A. Ghani, W. Polifke, Control of intrinsic thermoacoustic instabilities using hydrogen fuel, Proc. Combust. Inst. 38 (2021) 6077–6084.
[59] H. Kang, K. T. Kim, High-frequency combustion dynamics of multi-element lean-premixed hydrogen-air flame ensemble, Combust. Flame 233 (2021) 111585.
[60] S. Taamallah, Z. A. LaBry, S. J. Shanbhogue, A. F. Ghoniem, Thermo-acoustic instabilities in lean premixed swirl-stabilized combustion and their link to acoustically coupled and decoupled flame macrostructures, Proc. Combust. Inst. 35 (2015) 3273–3282.
[61] A. Datta, S. Gupta, S. Hemchandra, I. Chterev, I. Boxx, Impact of Hydrogen Addition on the Thermoacoustic Instability and processing vortex core dynamics in CH_4/H_2/Air technically premixed combustor, in: ASME Turbo Expo 2021, Paper No. GT2021-58794.
[62] A. Kushwaha, P. Kasthuri, S. A. Pawar, R. I. Sujith, I. Chterev, I. Boxx, Dynamical Characterization of Thermoacoustic Oscillations in a Hydrogen-Enriched Partially Premixed Swirl-Stabilized Methane/Air Combustor, in: ASME Turbo Expo 2021, Paper No. GT2021-60011.
[63] D. Moëll, D. Lörstad, X.-S. Bai, Les of hydrogen enriched methane/air combustion in the sgt-800 burner at real engine conditions, in: Turbo Expo: Power for Land, Sea, and Air, Vol. 51067, American Society of Mechanical Engineers, 2018, p. V04BT04A023.

[64] L. Y. Gicquel, G. Staffelbach, T. Poinsot, Large eddy simulations of gaseous flames in gas turbine combustion chambers, Prog. Energ. Combust. 38 (2012) 782–817.
[65] P. W. Agostinelli, Y. H. Kwah, S. Richard, G. Exilard, J. R. Dawson, L. Gicquel, T. Poinsot, Numerical and experimental flame stabilization analysis in the new spinning combustion technology framework, in: ASME Turbo Expo 2020, Paper No. GT2020-15035, p. V04AT04A058 (13 pages).
[66] P. Wolf, G. Staffelbach, A. Roux, L. Gicquel, T. Poinsot, V. Moureau, Massively parallel les of azimuthal thermo-acoustic instabilities in annular gas turbines, Comptes Rendus Mécanique 337 (2009) 385–394.
[67] E. Lo Schiavo, D. Laera, E. Riber, L. Gicquel, T. Poinsot, Effects of liquid fuel/wall interaction on thermoacoustic instabilities in swirling spray flames, Combust. Flame 219 (2020) 86–101.
[68] W. Meier, P. Weigand, X. Duan, R. Giezendanner-Thoben, Detailed characterization of the dynamics of thermoacoustic pulsations in a lean premixed swirl flame, Combust. Flame 150 (2007) 2–26.
[69] Z. Yin, P. Nau, W. Meier, Responses of combustor surface temperature to flame shape transitions in a turbulent bi-stable swirl flame, Exp. Therm. Fluid Sci. 82 (2017) 50–57.
[70] F. Duchaine, A. Corpron, L. Pons, V. Moureau, F. Nicoud, T. Poinsot, International Journal of Heat and Fluid Flow Development and assessment of a coupled strategy for conjugate heat transfer with Large Eddy Simulation : Application to a cooled turbine blade, Int. J. Heat Fluid Flow 30 (2009) 1129–1141.
[71] F. Duchaine, S. Mendez, F. Nicoud, A. Corpron, Conjugate heat transfer with Large Eddy Simulation for gas turbine components, Comptes Rendus Mécanique 337 (2009) 550–561.
[72] J. P. Legier, T. Poinsot, D. Veynante, Dynamically thickened flame LES model for premixed and non-premixed turbulent combustion, Proc. Summer Program, Cent. Turbul. Res. (2000) 157–168.
[73] B. Franzelli, E. Riber, L. Y. Gicquel, T. Poinsot, Large Eddy Simulation of combustion instabilities in a lean partially premixed swirled flame, Combust. Flame 159 (2012) 621–637.
[74] L. Haber, U. Vandsburger, A global reaction model for oh* chemiluminescence applied to a laminar flat-flame burner, Combust. Sci. Technol. 175 (2003) 1859–1891.
[75] Y. Hardalupas, M. Orain, Local measurements of the time-dependent heat release rate and equivalence ratio using chemiluminescent emission from a flame, Combust. Flame 139 (2004) 188–207.
[76] N. Docquier, S. Candel, Combustion control and sensors: a review, Prog. En. Combust. Sci. 28 (2002) 107–150.
[77] J. Lee, D. Santavicca, Experimental diagnostics for the study of combustion instabilities in lean premixed combustors, J. Propulsion Power 19 (2003) 735–750.
[78] B. Ayoola, R. Balachandran, J. Frank, E. Mastorakos, C. Kaminski, Spatially resolved heat release rate measurements in turbulent premixed flames, Combust. Flame 144 (2006) 1–16.
[79] K. Oberleithner, M. Stöhr, S. H. Im, C. M. Arndt, A. M. Steinberg, Formation and flame-induced suppression of the precessing vortex core in a swirl combustor: experiments and linear stability analysis, Combust. Flame 162 (2015) 3100–3114.
[80] C. D. Slabaugh, I. Boxx, S. Werner, R. P. Lucht, W. Meier, Structure and dynamics of premixed swirl flames at elevated power density, AIAA J. 54 (2016) 946–961.
[81] R. Zhang, I. Boxx, W. Meier, C. D. Slabaugh, Coupled interactions of a helical precessing vortex core and the central recirculation bubble in a swirl flame at elevated power density, Combust. Flame 202 (2019) 119–131.
[82] A. M. Steinberg, C. M. Arndt, W. Meier, Parametric study of vortex structures and their dynamics in swirl-stabilized combustion, Proc. Combust. Inst. 34 (2013) 3117–3125.
[83] A. M. Steinberg, I. Boxx, M. Stöhr, C. D. Carter, W. Meier, Flow–flame interactions causing acoustically coupled heat release fluctuations in a thermo-acoustically unstable gas turbine model combustor, Combust. Flame 157 (2010) 2250–2266.
[84] M. Stöhr, Z. Yin, W. Meier, Interaction between velocity fluctuations and equivalence ratio fluctuations during thermoacoustic oscillations in a partially premixed swirl combustor, Proceedings of the Combustion Institute 36 (2017) 3907–3915.
[85] P. Weigand, X. Duan, W. Meier, U. Meier, M. Aigner, C. Bérat, Experimental investigations of an oscillating lean premixed ch4/air swirl flame in a gas turbine model combustor, in: European Combustion Meeting, 2005.
[86] P. Weigand, W. Meier, X. Duan, M. Aigner, Laser based investigations of thermo-acoustic instabilities in a lean premixed gas turbine model combustor, in: ASME Turbo Expo 2006, Vol. 42363, Paper No. GT2006-90300, pp. 237–245.
[87] B. Franzelli, E. Riber, B. Cuenot, Impact of the chemical description on a Large Eddy Simulation of a lean partially premixed swirled flame, Comptes Rendus Mécanique 341 (2013) 247–256.
[88] D. Fredrich, W. P. Jones, A. J. Marquis, The stochastic fields method applied to a partially premixed swirl flame with wall heat transfer, Combust. Flame 205 (2019) 446–456.
[89] S. Roux, G. Lartigue, T. Poinsot, U. Meier, C. Bérat, Studies of mean and unsteady flow in a swirled combustor using experiments, acoustic analysis, and large eddy simulations, Combust. Flame 141 (2005) 40–54.
[90] J. Galpin, A. Naudin, L. Vervisch, C. Angelberger, O. Colin, P. Domingo, Large-eddy simulation of a fuel-lean premixed turbulent swirl-burner, Combust. Flame 155 (2008) 247–266.
[91] B. Fiorina, R. Vicquelin, P. Auzillon, N. Darabiha, O. Gicquel, D. Veynante, A filtered tabulated chemistry model for les of premixed combustion, Combust. Flame 157 (2010) 465–475.
[92] V. Moureau, P. Domingo, L. Vervisch, From large-eddy simulation to direct numerical simulation of a lean premixed swirl flame: Filtered laminar flame-pdf modeling, Combust. Flame 158 (2011) 1340–1357.
[93] G. Albouze, T. Poinsot, L. Gicquel, Chemical kinetics modeling and les combustion model effects on a perfectly premixed burner, Comptes Rendus Mécanique 337 (2009) 318–328.
[94] P. S. Volpiani, T. Schmitt, D. Veynante, Large eddy simulation of a turbulent swirling premixed flame coupling the TFLES model with a dynamic wrinkling formulation, Combust. Flame 180 (2017) 124–135.
[95] D. Fredrich, W. P. Jones, A. J. Marquis, Thermo-acoustic instabilities in the preccinsta combustor investigated using a compressible les-pdf approach, Flow Turbul. Combust. 106 (2021) 1399–1415.
[96] P. W. Agostinelli, B. Rochette, D. Laera, J. Dombard, B. Cuenot, L. Gicquel, Static mesh adaptation for reliable large eddy simulation of turbulent reacting flows, Phys. Fluids 33 (2021) 035141.
[97] O. Colin, M. Rudgyard, Development of High-Order Taylor-Galerkin Schemes for LES, J. Comput. Phys. 162 (2000) 338–371.
[98] F. Nicoud, H. B. Toda, O. Cabrit, S. Bose, J. Lee, Using singular values to build a subgrid-scale model for large eddy simulations, Phys. Fluids 23 (2011) 085106.
[99] H. Schlichting, K. Gersten, Boundary-layer theory, Springer Science & Business Media, 2003.
[100] F. Charlette, D. Veynante, C. Meneveau, A power-law wrin-

kling model for LES of premixed turbulent combustion: Part I - non-dynamic formulation and initial tests, Combust. Flame 131 (2002) 159–180.

[101] E. Ranzi, A. Frassoldati, A. Stagni, M. Pelucchi, A. Cuoci, T. Faravelli, Reduced kinetic schemes of complex reaction systems: Fossil and biomass-derived transportation fuels, Int. J. Chem. Kinet. 46 (2014) 512–542.

[102] Q. Cazères, P. Pepiot, E. Riber, B. Cuenot, A fully automatic procedure for the analytical reduction of chemical kinetics mechanisms for computational fluid dynamics applications, Fuel 303 (2021) 121247.

[103] T. Poinsot, S. Lele, Boundary conditions for direct simulations of compressible viscous flows, J. Comput. Phys. 101 (1992) 104–129.

[104] M. F. Modest, Radiative heat transfer, Academic press, 2013.

[105] W. L. Grosshandler, RADCAL: A Narrow Band Model for Radiation, NIST Tech. note 1402, 1993.

[106] J. M. Lourier, M. Stöhr, B. Noll, S. Werner, A. Fiolitakis, Scale Adaptive Simulation of a thermoacoustic instability in a partially premixed lean swirl combustor, Combust. Flame 183 (2017) 343–357.

[107] L. Rayleigh, The explanation of certain acoustical phenomena, Roy. Inst. Proc. 8 (1878) 536–542.

[108] K. Kashinath, I. C. Waugh, M. P. Juniper, Nonlinear self-excited thermoacoustic oscillations of a ducted premixed flame: bifurcations and routes to chaos, J. Fluid Mech. 761 (2014) 399–430.

[109] Y. Gong, D. Fredrich, A. J. Marquis, W. P. Jones, I. Boxx, Thermoacoustic Instabilities of Hydrogen-Enriched Partially Premixed Flames in a Swirl Combustor, in: ASME Turbo Expo 2021, Paper No. GT2021-60009, 2021, p. V03BT04A023.

[110] G. Aguilar, E. Æsøy, J. R. Dawson, in: Symposium on Thermoacoustics in Combustion: Industry meets Academia (SoTiC 2021).

[111] F. Nicoud, L. Benoit, C. Sensiau, T. Poinsot, Acoustic modes in combustors with complex impedances and multidimensional active flames, AIAA J. 45 (2007) 426–441.

[112] P. J. Schmid, Dynamic mode decomposition of numerical and experimental data, J. Fluid Mech. 656 (2010) 5–28.

[113] F. Richecoeur, L. Hakim, A. Renaud, L. Zimmer, Dmd algorithms for experimental data processing in combustion, Proc. Summer Program, Cent. Turbul. Res. (2012) 459–468.

[114] L. Magri, M. P. Juniper, J. P. Moeck, Sensitivity of the rayleigh criterion in thermoacoustics, J. Fluid Mech. 882 (2020) 1–11.

[115] E. Lo Schiavo, D. Laera, E. Riber, L. Gicquel, T. Poinsot, On the impact of fuel injection angle in Euler–Lagrange large eddy simulations of swirling spray flames exhibiting thermoacoustic instabilities, Combust. Flame 227 (2021) 359–370.

[116] D. Durox, T. Schuller, N. Noiray, S. Candel, Experimental analysis of nonlinear flame transfer functions for different flame geometries, Proc. Combust. Inst. 32 I (2009) 1391–1398.

[117] T. Schuller, T. Poinsot, S. Candel, Dynamics and control of premixed combustion systems based on flame transfer and describing functions, J. Fluid Mech. 894 (2020) P1.

[118] C. Willert, Stereoscopic digital particle image velocimetry for application in wind tunnel flows, Meas. Sci. Technol. 8 (1997) 1465–1479.